A pseudo three-dimensional electrochemical-thermal model of a cylindrical $LiFePO_4$/graphite battery

J. Chiew[a], C.S. Chin[b,c], W.D. Toh[a], Z. Gao[a], J. Jia[a], CZ. Zhang[c]

[a] *School of Engineering, Clean Energy Research Centre, Temasek Polytechnic, 21 Tampines Avenue 1, 529757, Singapore*
[b] *Faculty of Science, Agriculture, and Engineering, Newcastle University in Singapore, Singapore 599493*
[c] *School of Automotive Engineering; The State Key Laboratory of Mechanical Transmissions; Chongqing Automotive Collaborative Innovation Center, Chongqing University, Chongqing, China, 400044; czzhang@cqu.edu.cn*

Abstract

This paper introduces a pseudo three-dimensional electrochemical-thermal coupled battery model for a cylindrical Lithium Iron Phosphate battery. The model comprises a pseudo two-dimensional electrochemical cell model coupled with three-dimensional lumped thermal model. The cell is disassembled to obtain the physical dimensions of the cell components. The thermal characteristics of the cell are studied during the discharge process over a range of temperatures and discharge rates. The validity of the numerical model is demonstrated experimentally via a 26650 cylindrical Lithium Iron Phosphate/graphite battery cylindrical cell. Instead of infrared thermal images, series of regression models are utilized to quantify the thermal behavior at various depth of discharge under various discharge rates. The results demonstrated that the battery cell performs differently at a lower ambient temperature and lower discharge rate where the exothermic reactions are milder.

Keywords: Lithium-ion battery, Lithium Iron Phosphate/graphite battery, pseudo three-dimensional, electrochemical-thermal coupled model

1. Introduction

$LiFePO_4$/graphite lithium-ion batteries have gained significant traction in the electric automotive industry in the recent years mainly due to their high safety performance, flat voltage profile and low cost [1,2]. This means that these batteries are capable of providing reliable power, safely and economically. Although $LiFePO_4$ batteries have excellent thermal stability [3–6], they still suffer from thermal runaway like other lithium-ion type cells [7]. Thermal volatility is a major drawback in the lithium-ion [8] and sufficient knowledge of the thermal distribution and heat generation of the $LiFePO_4$ battery is necessary to avoid catastrophic thermal failure [9,10].

Lithium-ion battery numerical simulation is vital in the conceptual and fundamental understanding of the working mechanics in the battery cell [11]. Pioneering work performed by Doyle et al. [12] described the galvanostatic charge and discharge of a lithium polymer cell based on the porous electrode theory and

concentrated solution theory, also known as the pseudo-two-dimensional (P2D) model. Bernardi et al. [13] described the general energy balance of thermal modeling for battery systems.

Recent researches on numerical battery modeling and simulation can be categorized by battery chemistry, geometry and modeling approach. Majority of the literature describes the battery models of lithium manganese oxide ($LiMn_2O_4$, LMO) and lithium cobalt oxide ($LiCoO_2$, LCO) type cells of both prismatic and cylindrical configurations [14–23]. The minority of research papers are based on lithium iron phosphate ($LiFePO_4$, LFP) type cells where modeling approaches such as lumped thermal model [24], electrochemical-thermal coupled model [25], finite element thermal model [26] and even neural network approach [27] were used.

The trend of building battery packs out of small format cylindrical LFP battery cells has sparked a series of studies based on these characteristics. Researchers developed 2D electrochemical-thermal coupled battery models to study its thermal characteristics, capacity fade behavior, dynamic responses and electrical performances [28–33]. In electrochemical-thermal modeling, there are two approaches to modeling the cell's internal region, namely, homogenous or discrete. Capron et al. [34] performed a study which compared the two approaches. Although the discrete model demonstrated a more accurate temperature distribution, it was too computational costly. The homogenous modeling of internal cell region produced good accuracy results at a fast computational time and hence, is suitable for the study of a single cylindrical cell and/or multiple cells.

In recent years, the computation cost of numerical simulation has been greatly reduced with the advancement of computing. Studies based on 3D electrochemical-thermal coupled models have surfaced and demonstrated greater accuracy compared to its 2D equivalents and at affordable computational costs. Bahiraei et al. [35] presented a computational-affordable pseudo-3D model of a 4Ah NCA prismatic cell for electric vehicle thermal management applications. The presented model constitute of a 1D local electrochemical model coupled to a 3D lumped model. Xu et al. [36], Maheshwari et al. [37] and Lai et al. [38] presented pseudo-3D electrochemical-thermal models for prismatic LFP cells. These models consisted of a pseudo-2D electrochemical model coupled with a 3D heat transfer model and demonstrated a good agreement with experimental results. However, a pseudo-3D electrochemical-thermal coupled model was published by Saw et al. [31]. The model was developed to analyze the electrochemical and thermal behavior of a 18650 LFP cell over a range of temperatures and discharge rates. It also studied the effect of contact resistance between cell terminals and external connectors. In addition to the different type of cell used, the study was conducted at a constant ambient temperature of 298K (25^{o}C) that does not reflect the changing operating temperature of an actual battery cell.

Recently, the 26650 format cells have become more popular in the last few years due to rapid development and increased cell capacity to volume ratio. The form factor and material properties of the cell active materials contribute greatly to the electrochemical and thermal responses of the battery cell. Experimental based studies are often expensive and time-consuming. Hence, numerical mathematical modeling of the cell can help to reduce cost and time taken through the iterative design process where parameter can be easily varied by the user. With computational modeling and simulation, it provides a good understanding of the design limiting factors at minimal time and cost.

In this study, a pseudo-three-dimensional electrochemical-thermal model was developed for a commercially available 26650 cylindrical $LiFePO_4$/graphite battery. The cell was dismantled, and the physical components of the cell were measured. The electrochemical and thermal characteristics of the battery cell were studied through various discharge rates and ambient temperatures. The numerical simulation results were experimentally validated and the results exhibit good agreement. With the help of the model, the thermal behavior can be investigated and the contribution of different depth of discharge that leads to deviations in thermal performance is quantitatively assessed. The thermal infrared images were provided to examine the thermal distribution of the cell. Thus, the study provides the thermal behavior of the cell under different ambient temperature and discharge rates for actual implementation in the subsequent thermal management system of battery packs in electric vehicles, hybrid electric vehicles and underwater vehicles.

2. Electrochemical-thermal coupled model

2.1. Electrochemical model

The pseudo-three-dimensional electrochemical-thermal coupled model for a $LiFePO_4$ (lithium iron phosphate) lithium-ion battery cell is based on a pseudo-two-dimensional (P2D) electrochemical model coupled with a three-dimensional lumped thermal model. The pseudo-2D model derives from the electrochemical kinetics, charge and mass conservation in the solid and electrolyte phase whereas the 3D thermal model describes the heat transfer phenomenon. The electrochemical model provides the heat generation from the electrochemical reactions in the battery cell whereas the thermal model acts as a medium for heat transfer.

The P2D model is represented by the one-dimensional axis, x, and the radial dimension of the spherical dimension, r. The spherical particles are assumed to be distributed throughout the electrode and modeled in a two-dimensional plane. Unlike most 2D models, the particles in the P2D model are not directly coupled. Instead, the particles are coupled to the electrode through the radial direction, and the electrode is coupled

through the x-direction. The 3D lumped thermal model includes a cylindrical coordinate system which accounts for the orthotropic thermal conductivity of the battery cell.

Figure 1 is a representation of the cylindrical $LiFePO_4$ cell. The cell was disassembled to determine the exact build of the battery and to obtain the dimensions of the cell components. The cell consists of five layers (from left to right): negative current collector, a negative electrode, separator, a positive electrode, and positive current collector. The current collectors are usually copper at the negative electrode and aluminum at the positive electrode. The separator is a thin polyethylene film that electrically insulates the electrodes but conducts ions. The cell is rolled up into the battery can and filled with an electrolyte solution.

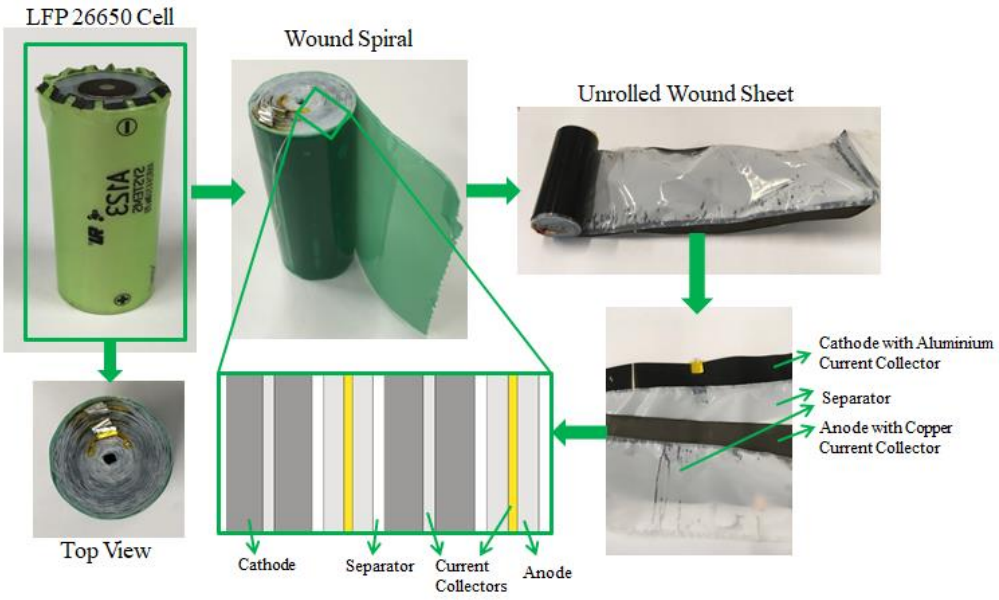

Figure 1: Cylindrical LFP battery geometry

During the discharging process, lithium ions migrate from the negative electrode to the positive electrode. During this process commonly described as deintercalation and interaction of lithium ions, electrons are released into the external circuit as shown in Figure 2. At the beginning of discharge, the lithium ions insert into the $FePO_4$ particle that causes the surface of the particle to be lithiated while the core remains delithiated. Two-phase regions are established during this process. Towards the end of discharge, the $LiFePO_4$ particle is completely lithiated and regains its status of a single phase region [39–42]. However, the proposed model does not consider the phase change process that takes place within the electrode. But is still capable of producing sufficiently accurate results [29,43].

The separator and electrolyte are non-conductors of electrons and only facilitate the movement of lithium ions. The positive and negative electrode active materials are $Li_{y-z}FePO_4$ (LFP) and Li_xC_6 respectively. The

electrolyte is 1.5 mol L^{-1} $LiPF_6$ (lithium hexafluorophosphate) dissolved in a mixture of 2:1 EC/DMC (ethylene carbonate/dimethyl carbonate).

The electrochemical reactions that occur between the electrode and electrolyte during discharge are as shown.

Negative electrode: $$Li_xC_6 \rightarrow Li_{x-z}C_6 + zLi^+ + ze^-$$

Positive electrode: $$Li_{y-z}FePO_4 + zLi^+ + ze^- \rightarrow Li_yFePO_4$$

where *x* is the number of moles of lithium present in the graphite structure of the negative electrode, *y* is the number of moles of lithium in the olivine structure of the iron phosphate ($FePO_4$) of the positive electrode, z is the number of moles of lithium taking part in the electrochemical reaction, Li^+ is the lithium ions and e^- is the electrons.

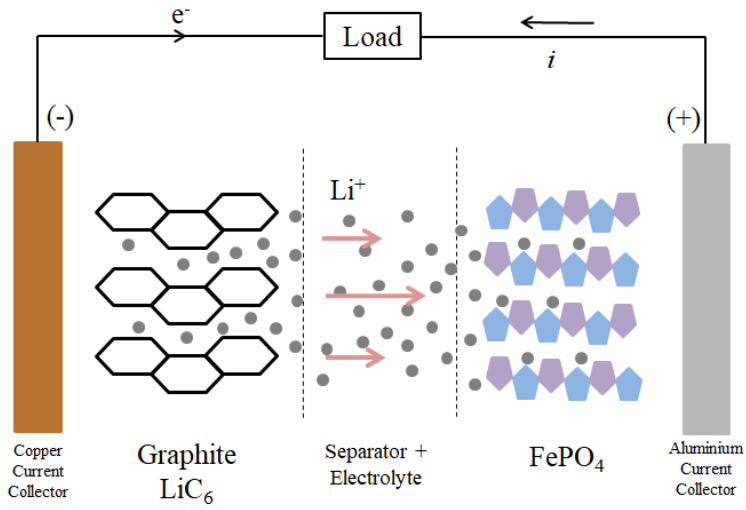

Figure 2: Schematic of a $LiFePO_4$ electrochemical cell

The electrochemical P2D model accounts for electrochemical kinetics, charge and mass conservation in the solid and electrolyte phase. The relationship between the P2D model and 3D thermal model is defined by the dual-directional coupling of heat generation calculation by the P2D model and the subsequent heat transfer through the battery materials in the 3D thermal model. The thermal model also includes ambient temperature changes and effects which affects the cell's electrochemical process and heat generation.

The electrochemical kinetic of lithium intercalation and deintercalation process utilizes the Butler-Volmer equation to calculate the local charge transfer current density. The charge conservation is described by the electron transport in the solid phase and the ionic transport of lithium ions in the electrolyte which follows the Ohm's law and concentrated solution theory, respectively. The concentrated solution theory follows the change

of concentration due to mass flux and reaction. For electron transport in the solid phase, it is necessary to capture the effect of the double layer capacitance at the electron/electrolyte interface, where two layers of ions are separated by a solvent layer which acts as a capacitor.

The mass conservation and balance of lithium through the electrode and electrolyte follows Fick's law in the spherical coordinate system. The electrolyte mass balance primarily considers diffusion due to concentration gradients and electron migration due to an applied electric field, while often ignoring the effect of inner convection due to a density gradient.

2.2. Electrochemical kinetics

The local charge transfer current density, j_n, is determined by the Butler-Volmer equation [31] as shown in Eq. (1). The Butler-Volmer equation describes the dependence of the electrode electrical current on the electrode potential.

$$j_n = j_0\left[\exp\left(\frac{\alpha_a F}{RT}\eta\right) - \exp\left(\frac{\alpha_c F}{RT}\eta\right)\right] \tag{1}$$

where j_0 is the exchange current density, α_a and α_c are the anodic and cathodic charge transfer coefficient, respectively, F is the Faraday's constant, R is the gas constant, T is the temperature and η is the local surface over potential.

The exchange current density, j_0, is the rate of reaction at the reversible potential when over potential is zero and reflects the electron transfer rates. It is calculated in Eq. (2) [31]:

$$j_0 = Fk_0 c_1^{\alpha_a}\left(c_{s,\max} - c_{s,surf}\right)^{\alpha_a} c_{s,surf}^{\alpha_c} \tag{2}$$

where k_0 is the reaction rate constant, $c_{s,max}$ is the maximum lithium concentration in the electrodes, $c_{s,surf}$ is the lithium concentration on the surface of the active material and c_s and c_l are the concentration of lithium in the active material particles and electrolyte, respectively.

Over potential is the potential difference between electrode potential and the equilibrium potential. The local surface over potential, η, is defined as [31]:

$$\eta = \phi_s - \phi_l - U_{eq} \tag{3}$$

where ϕ_s is the solid phase potential, ϕ_l is the electrolyte phase potential and U_{eq} is the open circuit potential of the electrode.

The open circuit potential of the electrode, U_{eq}, is dependent of the state-of-charge (SOC) and temperature which can be approximated with a Taylor's series expansion [36].

$$U_{eq} = U_{eq,ref} + \frac{\partial U_{eq}}{\partial T}\left(T - T_{ref}\right) = U_{eq,ref}\left(SOC, T_{ref}\right) + \frac{\Delta S(SOC)}{nF}\left(T - T_{ref}\right) \tag{4}$$

where SOC for both positive and negative electrodes is determined by the ratio of the concentration of lithium ions in the active material, Eq. (5).

$$SOC = \frac{c_s}{c_{s,\max}} \tag{5}$$

The equation of change in entropy, ΔS, is given as,

$$\Delta S = nF\left(\frac{\partial U_{eq}}{\partial T}\right) \tag{6}$$

where n is the number of electrons transferred.

2.3. Charge conservation

Electrical charge conservation is the principle that the net quantity electric charge is always conserved. The charge conservation in the positive and negative electrodes is governed by the following equations:

$$\nabla \cdot i_s + \nabla \cdot i_l = 0 \tag{7}$$

$$\nabla \cdot i_s = -S_a j_n \tag{8}$$

$$\nabla \cdot i_l = S_a j_n \tag{9}$$

where i_s is the electrical current density in the solid phase, i_l is the ionic current density in the electrolyte and S_a is the specific surface area.

The electron transport in the solid phase follows Ohm's law as shown in Eq. (10).

$$i_s = -\sigma_s^{eff} \nabla \phi_s \tag{10}$$

where σ_s^{eff} is the effective electronic conductivity in the solid phase material.

The ionic transport of lithium ions in the electrolyte is as shown in Eq. (11). The ionic current density in the electrolyte, i_l, consists of two terms. The first term follows Ohm's law while the second term accounts for the ionic concentrated solution effects.

$$i_l = -\sigma_l^{eff}\nabla\phi_l + \frac{2RT\sigma_l^{eff}}{F}\left(1+\frac{\partial \ln f_{\pm}}{\partial \ln c_1}\right)\left(1-t^+\right)\nabla\left(\ln c_l\right) \tag{11}$$

where σ_l^{eff} is the effective ionic conductivity of the electrolyte, $f_{\pm}$ is the average molar activity coefficient, t^+ is the transferring number of lithium ions and c_l is the concentration of lithium ions in the electrolyte.

2.4. Mass conservation

The law of conservation of mass states that the quantity of the mass in a closed system must be conserved over time. The composite electrodes are modeled after the porous electrode theory which means that each material in the electrode is represented by a volume fraction. Effective transport parameters such as the effective electrolyte diffusion, $D_{l,eff}$, the effective ionic conductivity of the electrolyte, $\sigma_{l,eff}$, and effective electronic conductivity of the electrode, $\sigma_{s,eff}$, are corrected with the Bruggeman tortuosity exponent, γ, to account for porosity and tortuosity of the electrode. The solid-phase particles are assumed to be uniformly distributed throughout the electrode which allows the electrochemical reaction to be treated as a homogeneous term.

The mass conservation of lithium ions in the spherical active material is described by Fick's law of diffusion in Eq. (12). Fick's law of diffusion states that the molar flux due to diffusion is proportionate to the concentration gradient.

$$\frac{\partial c_s}{\partial t} - \frac{1}{r^2}\frac{\partial}{\partial r}\left(r^2 D_s \frac{\partial c_s}{\partial r}\right) = 0 \tag{12}$$

where c_s is the concentration of lithium in the active material particles, t is the time, D_s is the diffusion coefficient of lithium in the active material and r is the radial coordinate inside a spherical particle.

The mass conservation of lithium ions in the electrolyte is described in Eq. (13).

$$\varepsilon_l \frac{\partial c_l}{\partial t} + \nabla \cdot J_l = \frac{s_a j_n}{F} \tag{13}$$

where ε_l is the electrolyte volume fraction and J_l is the molar flux of lithium ions. The RHS term goes to zero when applied to the separator.

The molar flux of lithium ions consist of two terms. The first term follows Fick's law while the second term accounts for electro-migration. The molar flux of lithium ions is represented by the following equation:

$$J_l = -D_l^{eff} \nabla c_1 + \frac{i_l t^+}{F} \tag{14}$$

where D_l^{eff} is the effective diffusion coefficient of the electrolyte.

2.5. Energy balance

The energy balance in the lithium ion battery consists of three heat generation source terms, of which, two are irreversible and the other is reversible. The total heat generated is the summation of the reversible reaction heat generation q_{rea} and the irreversible polarization heat generation q_{pol} and ohmic heat generation q_{ohm}. The energy balance is expressed by:

$$q_{rea} + q_{pol} + q_{ohm} = \rho C_p \frac{\partial T}{\partial t} + \nabla \cdot \left(-\lambda \Delta T\right) \tag{15}$$

where ρ is the density, C_p is the specific heat capacity and λ is the thermal conductivity. The RHS consists of two terms; the first term describes the heat generated by the battery cell and the second term describes the heat dissipated to the environment.

The reversible reaction heat generation can be calculated by the following equation which is directly proportional to entropy change:

$$q_{rea} = S_a j_n T \frac{\partial U_{eq}}{\partial T} \tag{16}$$

The reaction heat is due to the heat generated by the chemical reactions in the lithium-ion battery.

The irreversible polarization heat generation can be calculated by the following equation:

$$q_{pol} = S_a j_n \eta \tag{17}$$

A localized equilibrium between the lithium-ion potential in the electrode and the potential in the electrolyte exists in the battery in the presence of an open circuit voltage condition. This equilibrium is disrupted to release current into the external circuit. The energy used to break this equilibrium is dissipated as active polarization heat.

The irreversible ohmic heat generation can be calculated by the following equation:

$$q_{ohm} = -i_s \cdot \nabla \phi_s - i_l \cdot \nabla \phi_l \tag{18}$$

The ohmic heat generation consists of two terms. The first term accounts for the electrical heat generation in the solid phase while the second term accounts for the ionic heat generation in the electrolyte.

The heat dissipated to the environment as mentioned in Eq. (19) consists of heat transfer via convection and radiation. According to Newton's law of cooling and Stefan-Boltzmann's law of radiation, the energy balance and conservation is expressed by:

$$-\lambda \nabla T = -\alpha\left(T_{amb} - T\right) - \varepsilon\sigma\left(T_{amb}^4 - T^4\right) \tag{19}$$

where α is the convective heat transfer coefficient, ε is the emissivity of the battery surface, σ is the Stephen-Boltzmann constant, T and T_{amb} is the battery surface temperature and ambient temperature, respectively.

The natural convection heat transfer coefficient is taken to be 7.17 W m^{-2} K^{-1} and the emissivity of the battery surface is taken as ε = 0.8 [29]. However, due to the relatively low operating temperature range, the effect of radiation is minimal and can be neglected.

2.6. Temperature and concentration-dependent (dynamic) parameters

The temperature and concentration-dependent parameters define the non-linear characteristics of the electrochemical coupled model. These parameters are the reaction rate, the open circuit potential and entropy change, which are described in Eq. (4), ionic conductivity in the electrolyte and the diffusion coefficient in the electrode and electrolyte.

The temperature dependent reaction rate constant, k_0, follows the Arrhenius equation [13]. The Arrhenius equation defines the relationship between the activation energy and the rate of chemical reaction; how temperature affects the reaction rate.

$$k_0(T) = k_{0,ref} \exp\left[\frac{E_{aR}}{R}\left(\frac{1}{T_{ref}} - \frac{1}{T}\right)\right] \tag{20}$$

where $k_{0,ref}$ is the reaction rate constant at the reference temperature and E_{aR} is the reaction activation energy.

The concentration and temperature dependent ionic conductivity in the electrolyte, σ_l, which was based on the parameters of the $LiPF_6$ in EC/DMC (2:1) at 298K, is described as [29]:

$$\sigma_l(c_1,T)=1.12\times10^{-4}\begin{pmatrix}-8.2488+0.053248T-2.9871\times10^{-5}T^2+0.26235c_l-9.3063\\ \times10^{-3}T+8.069\times10^{-6}c_lT^2+0.220022c_l^2-1.765\times10^{-4}c_l^2T\end{pmatrix} \quad (21)$$

The temperature dependent diffusion coefficient in the solid phase is expressed as:

$$D_s(T)=D_{s,ref}\exp\left[\frac{E_{aD}}{R}\left(\frac{1}{T_{ref}}-\frac{1}{T}\right)\right] \quad (22)$$

where $D_{s,ref}$ is the diffusion coefficient of lithium in the active material at a reference temperature and E_{aD} is the diffusion activation energy.

The diffusion coefficient of lithium in the active material at the reference temperature is a function of SOC as seen below.

$$D_{s,ref}=3.9\times10^{-14}(1.5-SOC)^{3.5} \quad (23)$$

In this study, a simplified term for the diffusivity coefficient in the positive and negative electrode is taken.

$$D_{s,p}(T)=1.18\times10^{-18}\exp\left[\frac{E_{aD}}{R}\left(\frac{1}{T_{ref}}-\frac{1}{T}\right)\right] \quad (24)$$

$$D_{s,n}(T)=3.9\times10^{-14}\exp\left[\frac{E_{aD}}{R}\left(\frac{1}{T_{ref}}-\frac{1}{T}\right)\right] \quad (25)$$

The concentration and temperature dependent diffusion coefficient in the electrolyte is expressed as [30,36]:

$$D_1(c_1,T)=10^{\left(-4.43-\left(\frac{54}{T-229-0.005c_l}\right)-0.0022c_l\right)-4} \quad (26)$$

The thermodynamic factor of the electrolyte, v_l is expressed as [29]:

$$v_l(c_l,T)=0.601-0.24\sqrt{0.001c_l}+0.982\left(1-0.0052(T-294)\sqrt{10^{-9}c_l^3}\right) \quad (27)$$

As shown in Eq. (4), the open circuit potential (U_{eq}) and entropy change (ΔS) is dependent on the state of charge (SOC) and are determined by experimental methods. Eq. 27 and 28 represent the curves of U_{eq} vs. SOC at the reference temperature of 298K for both Li_yFePO_4 and Li_xC_6 electrodes [28,29].

$$U_{eq,p} = 3.4323 - 0.4828e^{-80.2493(1-y)^{1.3198}} - 3.2474\times10^{-6}e^{20.2645(1-y)^{3.8003}} + 3.2482\times10^{-6}e^{20.2645(1-y)^{3.7995}} \quad (27)$$

$$\begin{aligned} U_{eq,n} = {} & 0.6379 + 0.5416\mathrm{e}^{-305.5309\mathrm{x}} \\ & + 0.044\tanh\left(-\frac{\mathrm{x}-0.1958}{0.1088}\right) \\ & - 0.1978\tanh\left(\frac{\mathrm{x}-1.0571}{0.0854}\right) \\ & - 0.6875\tanh\left(\frac{\mathrm{x}-0.0117}{0.0529}\right) - 0.0175\tanh\left(\frac{\mathrm{x}-0.5692}{0.0875}\right) \end{aligned} \quad (28)$$

Eq. 29 and 30 represent the curves of ΔS vs. SOC at the reference temperature of 298K for both Li_yFePO_4 and Li_xC_6 electrodes [44,45].

$$\begin{aligned} \Delta\mathrm{S_p} = {} & -0.35376\mathrm{y}^8 + 1.3902\mathrm{y}^7 - 2.2585\mathrm{y}^6 + 1.9635\mathrm{y}^5 - 0.98716\mathrm{y}^4 + 0.28857\mathrm{y}^3 \\ & - 0.046272\mathrm{y}^2 + 0.0032158\mathrm{y} - 0.000019186 \end{aligned} \quad (29)$$

$$\begin{aligned} \Delta\mathrm{S_n} = {} & 344.1347148\left(\frac{\mathrm{e}^{-32.9633287\mathrm{x}+8.316711484}}{1+749.0756003\mathrm{e}^{-34.79099646\mathrm{x}+8.887143624}} - 0.8520278805\mathrm{x}\right. \\ & \left. + 0.362299229\mathrm{x}^2 + 0.2698001697\right) \end{aligned} \quad (30)$$

where *x* is the number of moles of lithium present in the graphite structure of the negative electrode (Li_xC_6), *y* is the number of moles of lithium in the olivine structure of the iron phosphate of the positive electrode (Li_yFePO_4).

The battery spatial and geometrical parameters, electrochemical kinetics, transport and thermal properties used in the numerical model and simulation are listed in Table 1.

2.7. Geometric calculations

Due to the spiral geometry of the active battery material, the thermal conductivity in the model is anisotropic; i.e. the thermal conductivity along the battery sheet is higher than the thermal conductivity in the normal direction of the sheet [46]. Therefore, the thermal conductivity in the radial and normal direction are calculated separately and included in the numerical model.

Thermal conductivity in the radial direction, normal to the battery sheet, is calculated by [46]:

$$k_{T,r} = \frac{\sum L_i}{\sum L_i / k_{T,i}} \tag{31}$$

Thermal conductivity along the length of the battery sheet is calculated by [46]:

$$k_{T,ang} = \frac{\sum L_i k_{T,i}}{\sum L_i} \tag{32}$$

where, L_i is the thicknesses of the different layers of the cell and $k_{T,i}$ is the collective thermal conductivities of the materials in the active material layers (i represents the number of layers in the cell).

The density, ρ and heat capacity, c_p of the active battery material are calculated similarly by [46]:

$$\rho = \frac{\sum L_i \rho_i}{L_i} \tag{33}$$

$$c_p = \frac{\sum L_i c_{p,i}}{\sum L_i} \tag{34}$$

The volume of active material, V_s in the spirally wound battery sheets which are necessary during the conversion of volumetric heat generation [W/m^3] to heat generation [W] can be calculated from [34]:

$$V_s = 2whL \tag{35}$$

where V_s is the volume of active material, w is the width of the active material layer, h is the height of the battery sheet and L is the length of the battery sheet or length of spirally formed by the wound battery sheet. The length of the battery sheet can be measured or calculated by:

$$L = \pi N\left(D + d/2\right) \tag{36}$$

where N is the number of layers, D is the outer diameter of the spiral and d is the inner diameter of the spiral.

Table 1: Battery parameters used in the numerical model

Parameter	Units	Negative Electrode	Separator	Electrolyte	Positive Electrode	Cu CC	Al CC	Ref.
Battery Geometric Parameters								
A_{cell}	m^2	0.1972						Estimated
ε_s		0.54			0.45			Adjusted
ε_l		0.33	0.54		0.332			[29]
δ_i	m	3.5×10^{-5}	2.0×10^{-5}		6.5×10^{-5}	1.0×10^{-5}	2.0×10^{-5}	Measured
$w_{0\%}$		0.0132			0.74			[33]
$w_{100\%}$		0.811			0.035			[33]
r_0	m	3.65×10^{-8}			3.5×10^{-6}			Estimated
Lithium ion Concentrations								
$c_{s,max}$	mol m^{-3}	31370			22806			[28,29]
$c_{l,0}$	mol m^{-3}			1200				[28,29,33]
c_s	mol m^{-3}	0.86 $c_{s,max}$			0.12 $c_{s,max}$			[29]
Kinetic and Transport Parameters								
α_a, α_c		0.5			0.5			Estimated
γ		1.5	1.5		1.5			Assumed
D_s	$m^2 s^{-1}$	Eq. (25)			Eq. (24)			Calculated
D_l	$m^2 s^{-1}$			Eq. (26)				Calculated
k_0	$m^{2.5} mol^{-0.5} s^{-1}$	3×10^{-11}			1.4×10^{-12}			[28,29]
E_{aR}	kJ mol^{-1}	20			30			[29]
σ_s	S m^{-1}	100			0.5			[28,29]
σ_l	S m^{-1}			Eq. (21)				Calculated
ν_l				Eq. (27)				Calculated
t^+			0.363					[12]
Battery Thermophysical Parameters								
λ	W $m^{-1} K^{-1}$	1.04	1.0	0.6	1.48	398	238	[46]
ρ	kg m^{-3}	2500	1200	1130	1500	8900	2700	[45,46]
C_p	J $kg^{-1} K^{-1}$	800	800	2055	800	3440	2420	[45,46]
Constants								
F	C mol^{-1}	96,487						
R	J $mol^{-2} K^{-1}$	8.314						
σ	W $m^{-2} K^{-4}$	5.67×10^{-8}						

3. Numerical simulation and experimental setups

3.1. Numerical simulation setup

A finite element method (FEM) based commercial software, COMSOL Multiphysics 5.2a, was used to solve the pseudo-3D electrochemical-thermal coupled model presented in this paper. The input of the model is an applied

current and atmospheric temperature. The outputs of the model are the battery output voltage and battery surface temperature distribution. The model automatically stops at the set cutoff voltage of 2.5V.

The PARDISO solver was chosen with a relative tolerance of 10^{-3} for all the variables; solutions were tested for mesh independence and the solution time for this model was approximately 1670 seconds by a computing platform with 4-core processors (2.60GHz) and a total of 2 x 8 GB RAM (random access memory). The mesh of the 3D model of the cell is composed of 133,783 elements with a minimum element quality of 0.006265.

3.1.1. Numerical model calibration and verification

The battery used in this experiment is the latest version of the A123 LFP 26650 series named ANR26650*M1*-B. The older model of the battery cell, ANR26650*M1*-A, was used in several other studies [28,29,32,33]. The main differences between the two models are as listed [47].

- Increased capacity from 2.3Ah to 2.5Ah nominal
- Reduced impendence, higher power
- Longer life
- Low self-discharge
- Improved aesthetics

The difference in charge capacity affects the numerical model which has to be validated and verified based on the physical changes of the cell. Other notable physical changes which contribute to the increased performance of the newer cell model are a) new separator and b) new cathode, which has been measured in Figure 1.

The charge capacity in both electrodes of the ANR26650*M1*-B cell can be calculated with Eq. (37) [33].

$$Q = \varepsilon_s F \delta_i A c_{s,\max} \left| w_{100\%} - w_{0\%} \right| \tag{37}$$

where Q is the charge capacity, ε_s is the active material volume fraction, F is Faraday's constant, A is the area of the electrode, $c_{s,max}$ is the maximum concentration of lithium in the active material and w is the number of moles of lithium present in the electrode.

Substituting the values from Table 1 into Eq. (37) gives the values of 2.50Ah for the negative electrode and 2.49Ah for the positive electrode; which is within the range of the nominal capacity of 2.5Ah and a minimum capacity of 2.4Ah as provided by the manufacturer.

3.2. Experimental setup (Thermocouple)

Commercially available 26650 $LiFePO_4$ battery cells (Ø26 x L65mm, A123 cylindrical LFP battery, capacity 2.5Ah, nominal voltage 3.3V, electrolyte $LiPF_6$ in EC/DMC 2:1) were used in the experiment. The charging of the battery was conducted using a DC power supply (GwINSTEK GPC-30600) at the recommended 2.5A to 3.6V CCCV (60 minutes) in laboratory conditions. The discharging experimental test was performed in a temperature chamber (Weiss WKL 34/40) and discharged to a programmable electronic load (KIKUSUI PLZ1004W) which was also used to collect electrical data. A K-type thermocouple was placed on the surface of the battery cell and temperature data was logged by a data acquisition unit (KEYSIGHT 34972A).

The battery cell was discharged under different current rates (1C, 2C, 3C and 4C) under a range of temperatures (293K, 298K, and 303K). Each experiment was performed on three different battery cells and the average was taken. The stop condition for the discharge was set to 2.5V to prevent damage to the cell and to affect the subsequent test results. The definition of discharge rate as per the standard IEC61434 is [31].

$$I_t = C/1h \tag{38}$$

where I_t is the discharge current in amperes and C is the measured capacity of the battery cell in ampere-hour. For example, C-rate of 2C of a 2.5Ah rated cell can provide 5A for half hour.

Figure 3 shows the schematic of the experimental setup (left) and actual experimental setup (right) which utilizes the thermocouple measurement method.

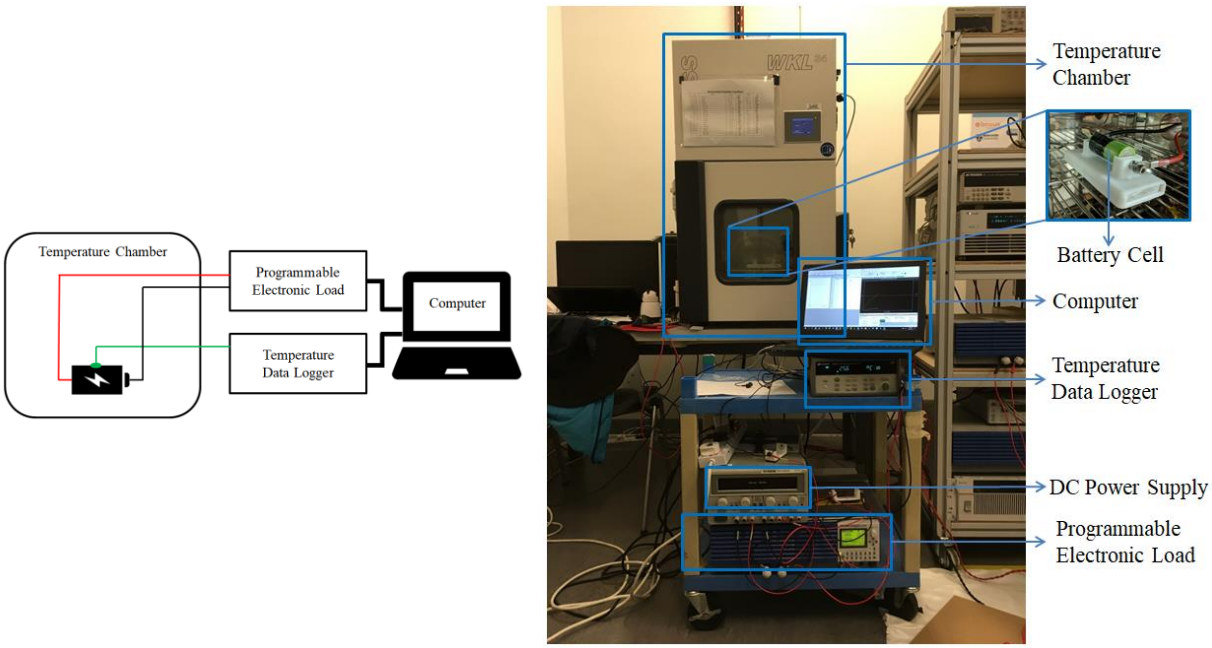

Figure 3: Schematic of the experimental setup (left), experimental setup (right) (Thermocouple)

The battery cell was allowed 30 minutes to rest after charging and 30 minutes in the temperature chamber to normalize its temperature before the discharge test began. A single K-type thermocouple was placed in the middle of the battery cell.

3.3. Experiment test (Infrared Thermal Imaging)

The ambient temperature test was performed in the laboratory environment where the temperature is kept approximately constant and discharged to a programmable electronic load (KIKUSUI PLZ1004W). A thermal infrared camera (FLUKE Ti400) was used to capture the temperature distribution of the battery cell which was wrapped in non-glossy black tape with a known emissivity of 0.95.

The battery cell was discharged under different current rates (1C, 2C, 3C and 4C) under the ambient laboratory temperature of 295.5K. Each experiment was performed on three different battery cells and the average was taken. The stop condition for the discharge was set to 2.5V to prevent damage to the cell and to affect the subsequent test results.

Figure 4 shows the schematic of the experimental setup (left), experimental setup (right) which utilizes infrared thermal imaging.

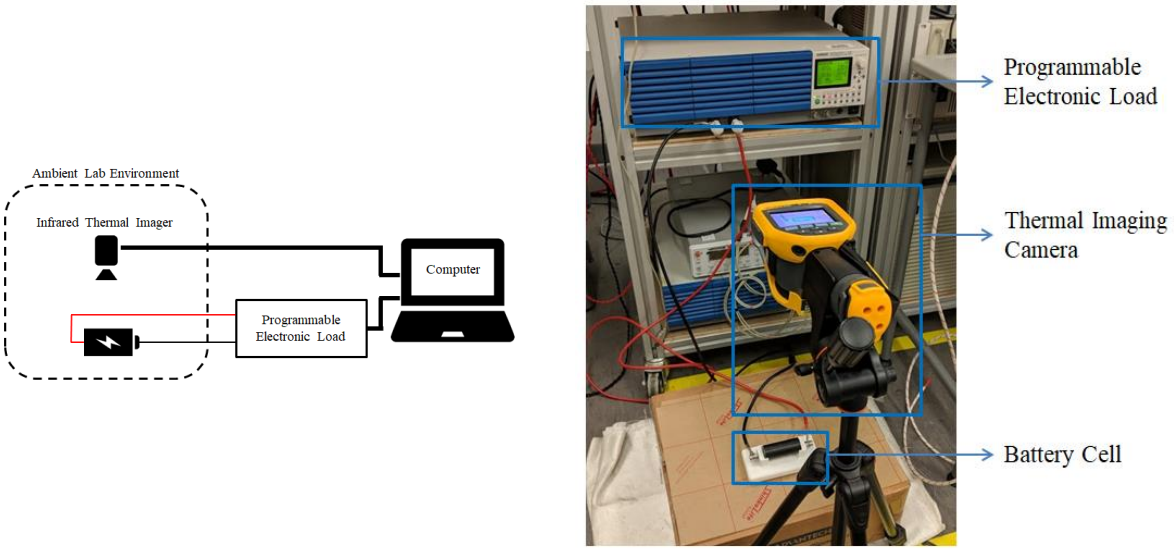

Figure 4: Schematic of the experimental setup (left), experimental setup (right) (IR Thermal Imaging)

The infrared thermal images were taken in intervals of 1% of the depth of discharge based on total discharge time. The images were processed via FLUKE's SmartView infrared imaging analysis and reporting software.

3.4. Uncertainty analysis

An uncertainty analysis was performed on the two measurement methods, thermocouple measurement and infrared thermal imaging, to quantify the uncertainties and errors in the experiment. The k-type thermocouple was used to measure the surface temperature at the middle of the battery cell and has an error of ±2.2 K or ±0.75%, whichever is greater. The thermocouple is attached to a data acquisition unit, KEYSIGHT 34972A, which has a collective measurement error of ±0.53K [48]. Therefore, the total uncertainty for the temperature measurement via k-type thermocouple is approximately ±2.73K. The infrared thermal imager was used to display the temperature distribution on the surface of the battery cell at laboratory environment. It has a measurement uncertainty of ±2K or ±2%, whichever is greater. The calculated maximum error in this study is approximately ±2K.

4. Results and Discussion

Numerical simulations were performed for the 3D cylindrical LFP battery under 1C, 2C, 3C and 4C discharge rates at 293K, 298K, and 303K. The study aims to understand the thermal characteristics of the cell at different ambient temperatures during discharging. The results are based on the depth of discharge of the cell, which is

used to describe how much the battery has been discharging; where “0” stands for fully charged and “1” stand for fully discharged.

4.1. Model validation

The proposed electrochemical-thermal numerical model was put through a two-step validation process. First, the model is validated by the experiment data of the battery voltage against the depth of discharge at a constant temperature of 298K. Next, the thermal model is validated by the experiment data of the battery surface temperature against the depth of discharge at various discharge rates. Lastly, the thermal is validated by the experiment data of the battery surface temperature against the depth of discharge at various ambient temperatures.

4.2. Electrochemical validation

The electrochemical performance of the battery model is validated via the battery voltage during the discharge process under the various discharge rates of 1C, 2C, 3C and 4C under the constant ambient temperature of 298K. The graph is plotted as voltage in Volt (V) against the depth of discharge (DoD) where “0.0” is considered fully charged and “1.0” as fully discharged. Figure 5 shows the voltage curve against the depth of discharge of the battery cell during discharging at 298K.

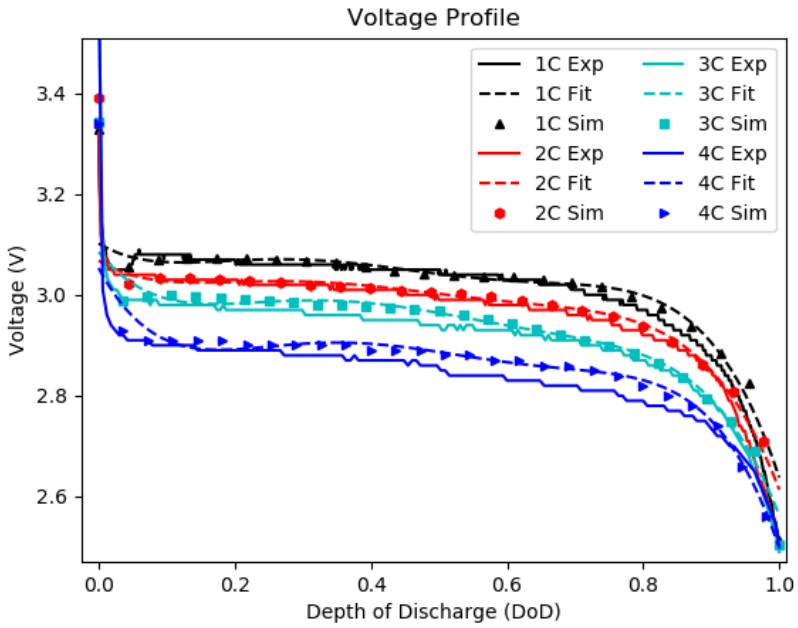

Figure 5: Voltage curve at 298K (Simulation vs. experimental results)

The comparison graph between the simulation and experiment demonstrates a good agreement. Nonetheless, there are slight discrepancies between them. The RMSE (root mean squared error) are 0.024, 0.022, 0.030 and 0.036 through the range of discharge rates respectively.

The errors are mainly observed in the discharge voltage plateau from 20% to 70% DoD. The errors could be due to the differences in open circuit voltage and entropy values of both Li_yFePO_4 and Li_xC_6 electrodes which were obtained from published literature instead of actual measured values. Some battery parameters used in the simulation in Table 1 were also values obtained from literature and adjusted from a similar battery make and model with a lower capacity. The voltage drop in the cables of the experimental setup also adversely affects the results.

The voltage curves of the numerical model were curve-fitted by fifth order polynomial and resulted in four equations respective the rates of discharge in ascending order as shown below.

$$U_{1C} = 3.10 - 0.81DoD + 6.01DoD^2 - 18.35DoD^3 + 23.62DoD^4 - 10.94DoD^5 \quad (38)$$

$$U_{2C} = 3.07 - 0.81DoD + 5.42DoD^2 - 15.60DoD^3 + 19.40DoD^4 - 8.86DoD^5 \quad (39)$$

$$U_{3C} = 3.09 - 1.69DoD + 9.89DoD^2 - 25.12DoD^3 + 28.17DoD^4 - 11.77DoD^5 \quad (40)$$

$$U_{4C} = 3.05 - 2.55DoD + 14.35DoD^2 - 35.29DoD^3 + 38.90DoD^4 - 15.96DoD^5 \quad (41)$$

The voltage curves obtained from the numerical model have been simplified into equations which may be implemented in battery management systems etc. The fifth polynomial curves accurately represent the initial voltage drop when connected to a load from 0.05 to 0.1 DoD; however, they are not able to represent the initial battery nominal voltage of 3.3V.

4.3. Thermal validation

The thermal validation has been spilt into two portions, namely, temperature profiles at a) ambient temperature and b) discharge rate. The validation process consists of a comparison between the experimental and simulation results.

4.3.1. Thermal validation by ambient temperature

Figure 6 shows the temperature profile of the battery in the various ambient temperatures of 293K, 298K and 303K. The graphs are plotted as the temperature in Kelvin (K) against the depth of discharge (DoD) where "0.0" is considered fully charged and "1.0" as fully discharged.

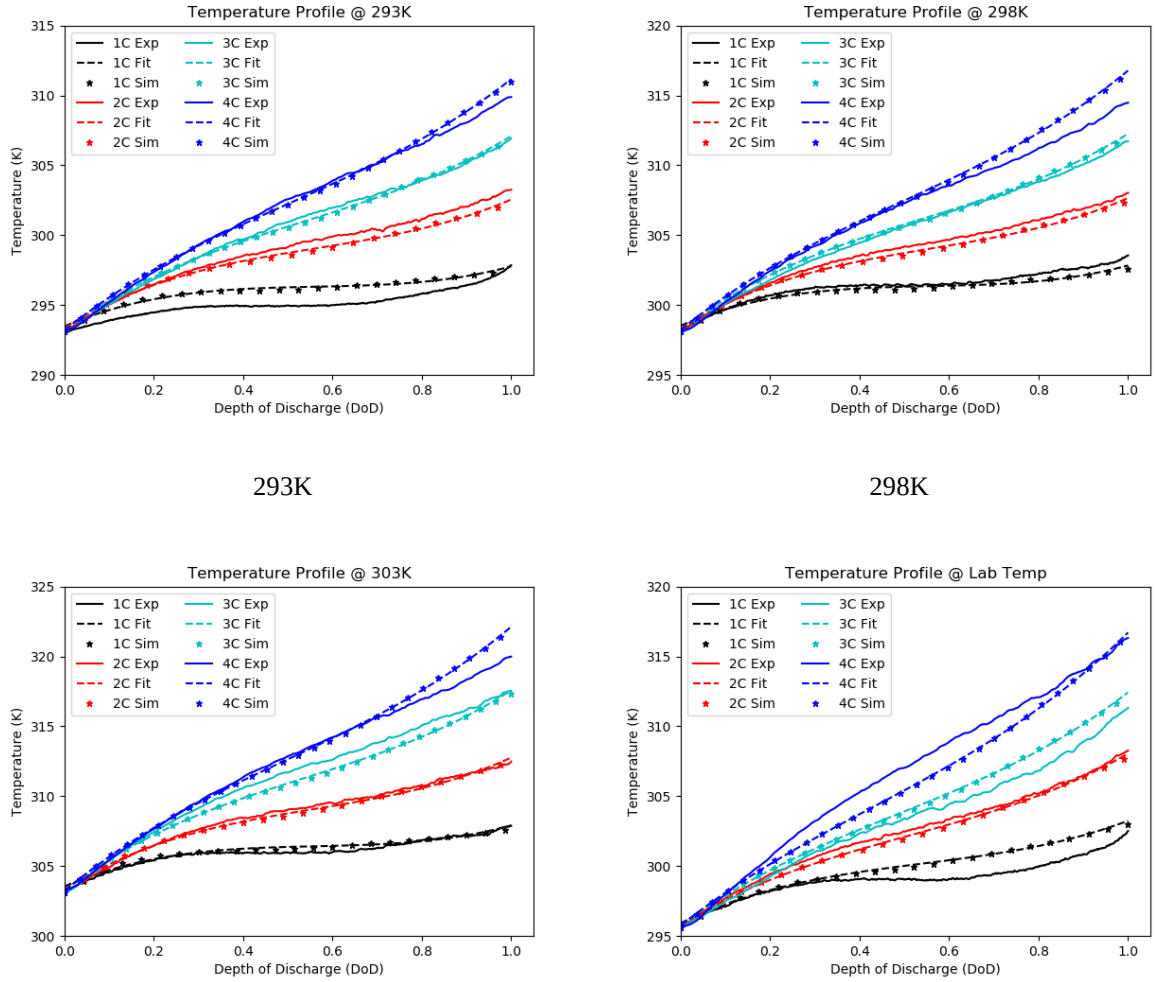

293K 298K

303K Lab Temp (295.5K)

Figure 6: Temperature profile at 293K, 298K, 303K and laboratory temperature

At an ambient temperature of 293K, the main discrepancies observed occur at the discharge rates of 1C where the simulation temperature is higher than the experimental temperature. The results at the other discharge rates demonstrate a good agreement between the experiment and the numerical model. The RMSE are 1.02, 0.52, 0.27 and 0.41 respectively through the range of discharge rates of 1C, 2C, 3C and 4C. At higher discharge rates of 4C, the temperature profile gravitates towards a linear characteristic where the temperature plateau from DoD 0.3 to 0.7 is absent.

The temperature profile curves (at 293K) of the numerical model were fitted by a third order polynomial. The equations shown below are organized by the discharge rates of 1C, 2C, 3C and 4C respectively.

$$T_{1C} = 293.49 + 13.78DoD - 23.36DoD^2 + 13.87DoD^3 \quad (42)$$

$$T_{2C} = 293.39 + 19.86DoD - 25.96DoD^2 + 15.27DoD^3 \quad (43)$$

$$T_{3C} = 293.27 + 22.92DoD - 23.73DoD^2 + 14.64DoD^3 \quad (44)$$

$$T_{4C} = 293.21 + 25.53DoD - 22.36DoD^2 + 14.78DoD^3 \quad (45)$$

The temperature curves obtained from the numerical model were simplified into cubic equations which could be implemented in battery thermal management systems etc. As seen in Figure 6, these cubic equations accurately represent the thermal characteristics from the exponential temperature increase from DoD 0.0 to 0.3, the plateau from DoD 0.3 to 0.7, and the following temperature rises from DoD 0.7 to the end of discharge. The R^2 values of the fitted curve range from 0.996 to 0.869.

At 298K, the results demonstrate a good agreement at all discharge rates, apart from the simulation temperature at a discharge rate of 4C at the end of the discharge cycle. The RMSE are 0.32, 0.39, 0.31 and 0.88 respectively through the range of discharge rates of 1C, 2C, 3C and 4C. The results obtained at the ambient temperature of 298K are slightly more accurate than that of ambient temperatures of 293K and 303K due to the open circuit potential and entropy change of the electrodes. These parameters were obtained at the reference temperature of 298K. Therefore the errors can be attributed to the experimentally obtained values of open circuit potential and entropy change of the electrodes at a reference temperature of 298K.

The temperature profile curves(at 298K) of the numerical model were fitted by a third order polynomial. The equations shown below are organized by the discharge rates of 1C, 2C, 3C and 4C respectively.

$$T_{1C} = 298.53 + 13.79DoD - 23.37DoD^2 + 13.89DoD^3 \quad (46)$$

$$T_{2C} = 298.34 + 19.95DoD - 26.00DoD^2 + 15.38DoD^3 \quad (47)$$

$$T_{3C} = 298.27 + 24.06DoD - 26.11DoD^2 + 16.05DoD^3 \quad (48)$$

$$T_{4C} = 298.23 + 26.10DoD - 22.82DoD^2 + 15.26DoD^3 \quad (49)$$

The temperature curves obtained from the numerical model were simplified into cubic equations which could be implemented in battery thermal management systems etc. As seen in Figure 6, these cubic equations accurately represent the thermal characteristics of the cell through all discharge rates. The R^2 values of the fitted curve range from 0.996 to 0.871.

Figure 6 shows the temperature profile of the battery at the ambient temperature of 303K. Similar to the results at 298K, the cell temperature at the end of the 4C discharge rate showed some inconsistency. An error was also observed at the 3C discharge rate where the experiment result produced a slightly higher temperature at a depth of discharge from 0.2 to 0.6. The RMSE are 0.23, 0.22, 0.60 and 0.68 respectively through the range of discharge rates of 1C, 2C, 3C and 4C. At the higher discharge rate of 3C, is it observed that the temperature of the cell does not come to a plateau as expected from DoD 0.3 to 0.7 as evident in the lower discharge rates of 1C, in fact, it increases. It could be due to the adjustment of ambient temperature in the temperature chamber controller.

The temperature profile curves (at 303K) of the numerical model were fitted by a third order polynomial. The equations shown below are organized by the discharge rates of 1C, 2C, 3C and 4C respectively.

$$T_{1C} = 303.55 + 13.89DoD - 23.46DoD^2 + 13.93DoD^3 \quad (50)$$

$$T_{2C} = 303.37 + 20.21DoD - 26.78DoD^2 + 15.96DoD^3 \quad (51)$$

$$T_{3C} = 303.28 + 24.45DoD - 26.51DoD^2 + 16.36DoD^3 \quad (52)$$

$$T_{4C} = 303.24 + 26.51DoD - 23.15DoD^2 + 15.52DoD^3 \quad (53)$$

The temperature curves obtained from the numerical model were simplified into cubic equations which could be implemented in battery thermal management systems etc. As seen in Figure 6, these cubic equations accurately represent the thermal characteristics of the cell. These equations enable the user to predict the temperature of the cell at different depth of discharge. The R^2 values of the fitted curve range from 0.996 to 0.873.

In the case of the approximately consistent ambient temperature, the battery model performed relatively well. The errors observed are mainly due to the unknown convection value as well as experiment errors which were not observed in the other experiments in a constant temperature environment. The temperature curve at 4C discharge rate displayed an uncharacteristic increase in the temperature gradient from 0.3 to 0.7 DOD. The uncertainties can be attributed to the method of temperature control in the laboratory where an on/off thermostat

is used. The RMSE are 0.99, 0.33, 0.84 and 1.13 respectively through the range of discharge rates of 1C, 2C, 3C and 4C.

The temperature profile curves of the numerical model were fitted by a third order polynomial. The equations shown below are organized by the discharge rates of 1C, 2C, 3C and 4C respectively.

$$T_{1C} = 295.92 + 15.51DoD - 21.09DoD^2 + 12.90DoD^3 \quad (54)$$

$$T_{2C} = 295.82 + 19.65DoD - 21.00DoD^2 + 13.57DoD^3 \quad (55)$$

$$T_{3C} = 295.78 + 23.39DoD - 21.77DoD^2 + 15.03DoD^3 \quad (56)$$

$$T_{4C} = 295.76 + 25.23DoD - 19.35DoD^2 + 15.07DoD^3 \quad (57)$$

The temperature curves obtained from the numerical model were simplified into cubic equations which could be implemented in battery thermal managements systems etc. As seen in Figure 6, these cubic equations accurately represent the thermal characteristics of the cell. The R^2 values of the fitted curve range from 0.995 to 0.975. The purpose of these equations in the unstable lab environment is to involve some real-world environment as well as test the accuracy and robustness of the numerical model.

4.3.2. Thermal validation by discharge rates

Figures 7 show the temperature profile of the battery by the discharge rates of 1C, 2C, 3C and 4C. The graphs are plotted as the temperature in Kelvin against the depth of discharge (DoD) where "0.0" is considered fully charged and "1.0" as fully discharged.

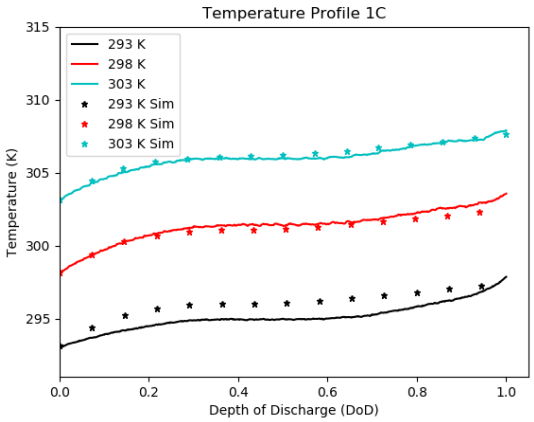

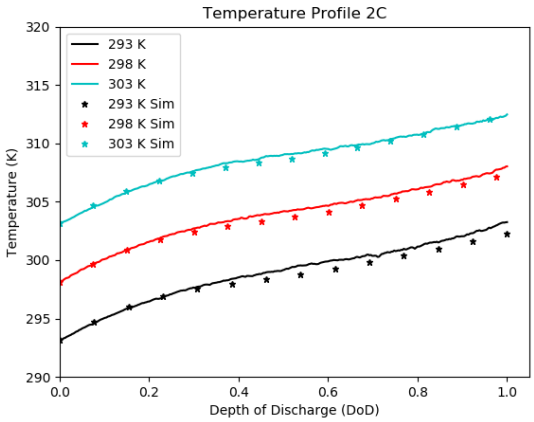

Discharge rate of 1C

Discharge rate of 2C

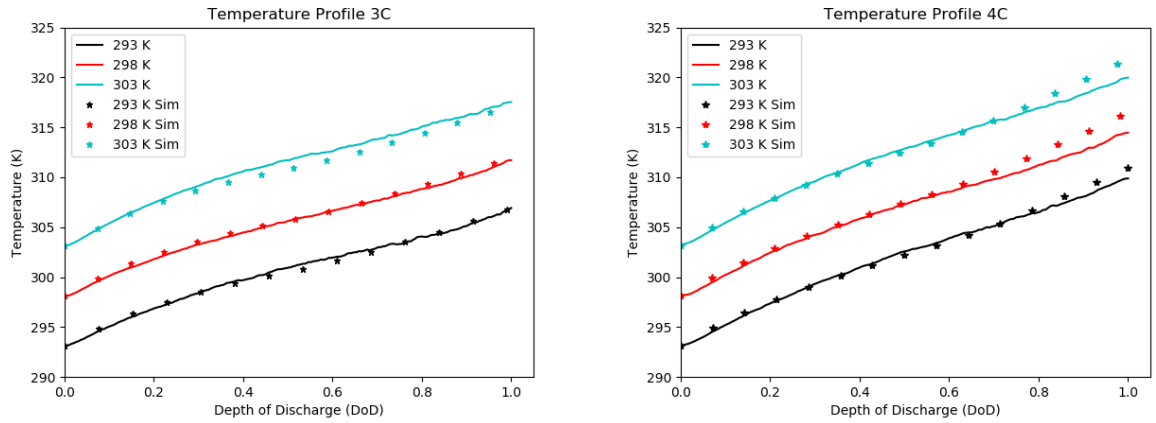

Discharge rate of 3C

Discharge rate of 4C

Figure 7: Temperature profiles at various discharge rates

As seen in Figure 7, the temperature profiles were organized by the discharge rates of 1C, 2C, 3C and 4C. The errors observed in Figure 6 remain unchanged. However, the errors are more pronounced in the 4C discharge rate as most results demonstrate a similar error at the end of the discharge. The simulation temperature ends higher compared to the experiment. Overall, the results agree with one all the ambient temperatures and discharge rates.

4.3.3. Thermal validation by infrared thermal imaging

The battery cell was discharged under ambient temperature in the laboratory as described in Figure 6. The temperature data in the experiment was captured by an infrared thermal imager. Similar boundary conditions were input in the battery model. The results were compared and showed a good agreement.

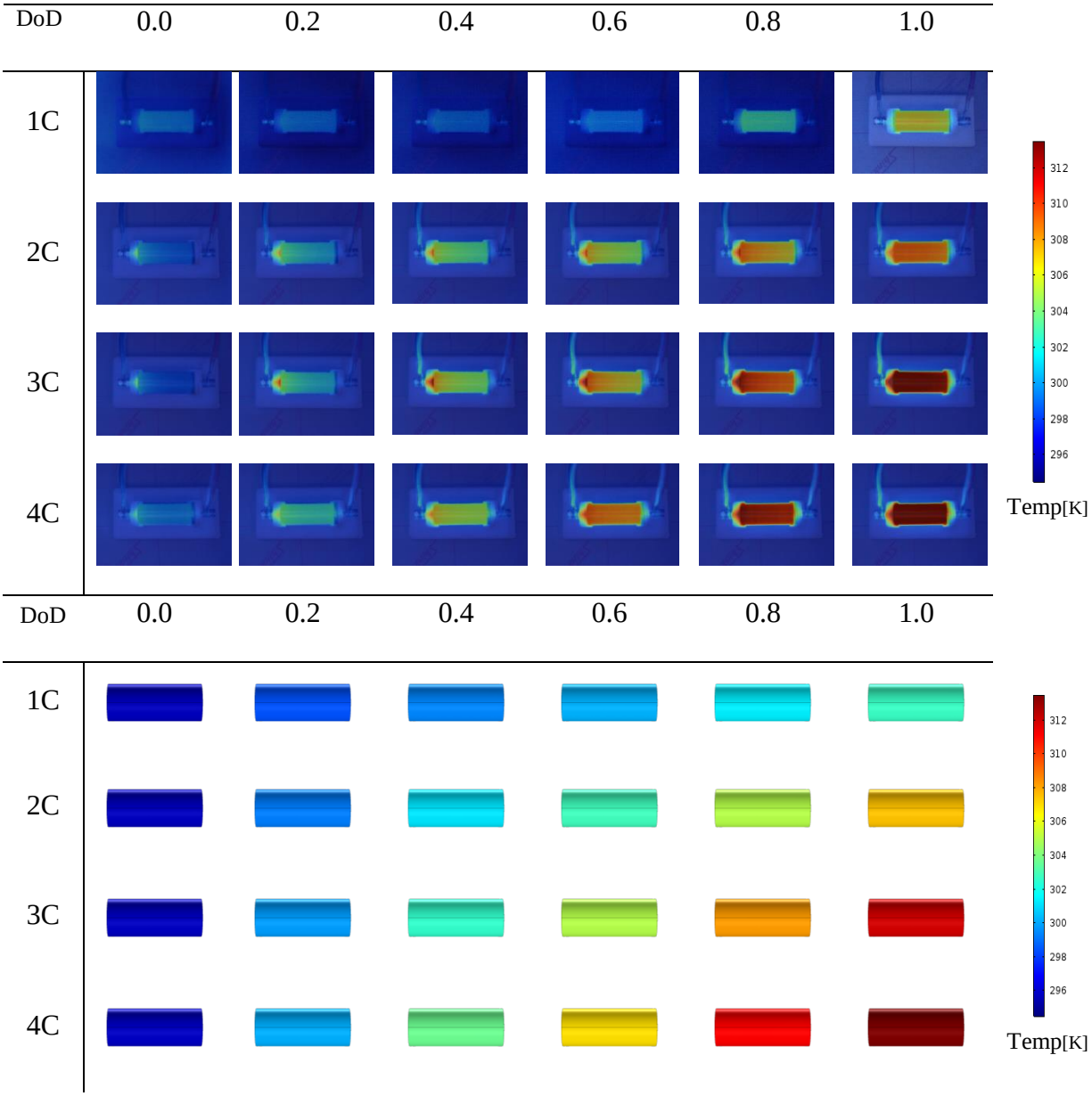

Figure 8: Simulation results at lab temperature of 295.5K

Figure 8 shows the infrared thermal images and simulation results at laboratory temperature at the various discharge rates, organized by the depth of discharge from 0 to 1 by intervals of 0.2. The heat generation and temperature gradient of the battery cell at 1C are significantly lower than that at higher discharge rates as agreed upon in Figure 7.

Heat transfer from the negative electrode of the battery cell to the connector on the rig is seen in the infrared thermal images. At higher discharge rates and DoD, the wires also get heated up due to the ohmic effect. However, the simulation model only considered heat transfer and distribution on the battery. Itcontributed to the errors between the experiment and simulation model seen in Figure 6.

The location of the thermocouple was placed in the middle of the cell as seen in Figure 3. Due to the external heat generation from the battery terminal connector, the negative electrode of the cell tends to get heated up first. The maximum temperature gradient between the positive and negative electrodes of the cell was recorded to be approximately 1.5K and the average temperature gradient was 0.5K. The middle of the battery cell was an average of the temperatures of both electrodes.

The usage of the infrared thermal imager allows the heat generation process through the depth of discharges over various discharge rates to be captured. The thermal images revealed external sources of heating and heat contributions could not be detected even by several thermocouples. These images aid in the visualization of the heat generation and distribution of the battery cell that is valuable in real-world applications in developing a battery thermal management system at the early stage of the design. Hence, the regression ambient temperature profiles vs. different DoD under the various depth of discharge are useful in the electrochemical-thermal modeling.

4.4. Results analysis

The errors observed in the comparison study between experiment and numerical model are due to measurement errors, assumed heat transfer coefficient, assumptions in the numerical model and neglected radiant heat loss. Some of the input values of the numerical model were measured or adjusted values for this particular battery model and values from published literature due to lack of sufficient cell information. There could have been compiled inaccuracies which contributed to the overall observable errors. Table 2 shows the root mean squared error (RMSE) between the experiment and simulation results.

Table 2: RMSE values for thermal validation

RMSE values	1C	2C	3C	4C
293K (20^{o}C)	1.02	0.52	0.27	0.41
298K (25^{o}C)	0.32	0.39	0.31	0.88
303K (30^{o}C)	0.23	0.22	0.60	0.68

The error observed in 1C discharge rate at 293K produced an RSME value of 1.02 which is significantly higher than the others. This observed error may be attributed to experimental issues. As seen in Figure 7, a comparison can be made between the temperature profiles of 1C discharge rates over the range of temperatures. At 293K of

1C discharge rate, the numerical model produced a visibly lower temperature curve as compared to the experiment results, which is uncharacteristic as compared to the other 1C discharge curves over the other ambient temperatures.

At the lower ambient temperature and lower discharge rates, the exothermic battery chemical reactions of the cell are less violent which results in lower rate of heat generation and lower temperature increase from the ambient environment. The endothermic behavior of the cell is also more prominent as compared to higher discharge rates. The $LiFePO_4$/graphite type cell consists of an electrode pairing that cancels reversible heat that contributes further to the reduction of overall heat generation [49].

At discharge rates of 4C, the RMSE values are slightly higher which is attributed to the increased temperature of the numerical model towards the end of discharge as shown in Figure 7. The numerical model was expected to produce a lower temperature as compared to the experiment results as contact resistance between the connectors, and battery terminals had been neglected. The electrical contact resistance would have been the rationale behind the temperature rise. However, in this case, it could be due to the approximated values of the entropy change of the electrode pair and/or the assumed natural heat transfer coefficient in the temperature chamber.

Towards the end of discharge from DoD 0.8 onwards, it is observed that temperature rises more rapidly due to the increase of internal resistance of the battery cell where the positive $FePO_4$ electrode is filled with lithium ions. It also signifies that the cell is fully discharged. The increased internal resistance of the cell can be seen in the voltage curve where a rapid voltage drop at the end of the discharge.

Comparing the heat distribution and contribution from the infrared thermal images and simulation numerical model in Figure 8, the ohmic heat contribution from the electrical contact resistant is neglected. The numerical model demonstrates an averaged cell-body temperature. However, the model shows a temperature gradient between the inner cell temperature and the surface temperature due to the anisotropic nature of the active battery material.

The infrared thermal images demonstrated the imbalance of temperatures at both terminals. The thermal conductivity of the battery cell is primarily dictated by the material of the current collector, where the negative current collector is made of copper and the positive current collector is made of aluminum. The heat generation at the negative terminal is caused by the flow of electrons and contact resistance while the heat generation at the

positive terminal is a result ohmic heating due to the lower thermal conductivity of the aluminum foil current collector.

The non-uniform temperature distribution of the battery cell shown in the infrared thermal images suggests that the placement of the thermocouple on the surface of the battery is important in reviewing the true averaged temperature of the cell. Hence, the errors observed in the experiment could be due to the improper placement of the thermocouple. The physical design of the battery holder also contributes to the heat accumulation underneath the battery cell.

The observable limitation of the numerical model is attributable to the temperature dynamic parameters such as the open circuit potential and entropy change of the electrodes. These parameters are usually experimentally attained at a reference temperature Therefore, when the battery cell was discharged at another ambient temperature, the results demonstrated small errors. Nevertheless, the results and numerical model show a fairly accurate model to study the thermal behavior of DoD at different ambient temperature and discharge rate.

5. Conclusion

In this paper, a three-dimensional electrochemical-thermal coupled model of a commercial 26650 $LiFePO_4$ battery was developed to study the thermal characteristics of the cell. The model was tested and validated at different discharge rates and ambient temperatures. The proposed numerical approach consists of a pseudo-two-dimensional electrochemical model coupled with a three-dimensional thermal lumped model. Good agreement between the numerical simulation and experiment results was achieved for both electrochemical validations via the discharge voltage curves and thermal validation via surface temperature monitoring. The results demonstrate an accurate and computationally efficient mode which provides good understanding of the thermal behavior of the cell under different ambient temperature and discharge rates. The model is suitable for the implementation in a battery thermal management system design of battery packs. As compared to the solving time of the numerical model that took around 1670s using COMSOL software under the various current and ambient temperatures, the curve fitted equations provide a mean to estimate the voltage, depth-of-discharge, cell temperature or/and ambient temperature for subsequent design and implementation stage for electric vehicles. Hence, it is not necessary to always simulate the cell model using the COMSOL software.

For future works, an expansion of the numerical model will include lower discharge rates at smaller intervals to study the exothermic and endothermic behavior of the cell. The numerical model will be further validated against a mathematic model via analytic methods leveraging on equations (1) – (37) and tested under a dynamic

and realistic load current profile. The numerical model will be expanded from a single cell study to a battery stack/matrix of multiple arrangements that will be put through various test conditions with different temperatures and various charge and discharge rates.

Conflicts of Interest

The authors declare no conflict of interest.

Nomenclature

A	area of the electrode	m^2
c_s	concentration of lithium in the active material particles	mol m^{-3}
c_l	concentration of lithium in the electrolyte	mol m^{-3}
$c_{s,max}$	maximum concentration of lithium in the active material	mol m^{-3}
$c_{s,surf}$	surface concentration of lithium in the active material	mol m^{-3}
C_p	specific heat capacity	J kg^{-1} K^{-1}
D_s	diffusion coefficient of lithium in the active material	m^2 s^{-1}
D_l	diffusion coefficient of electrolyte	m^2 s^{-1}
E_{aD}	diffusion activation energy	kJ mol^{-1}
E_{aR}	reaction activation energy	kJ mol^{-1}
E_{cell}	working voltage of the battery	V
$f_{\pm}$	average molar activity coefficient	
F	Faraday's constant (96,487 C mol^{-1})	C mol^{-1}
i	applied current density of the battery	A m^{-2}
i_s	electrical current density in solid phase	A m^{-2}
i_l	ionic current density in the electrolyte	A m^{-2}
j_0	exchange current density	A m^{-2}
j_n	local charge transfer current density	A m^{-2}
J_l	molar flux of lithium ion	mol cm^{-2} s^{-1}
k_0	reaction rate constant	$m^{2.5}$ $mol^{-0.5}$ s^{-1}
n	number of electrons transferred	
q	volumetric heat generation	W m^{-3}
q_{ohm}	ohmic volumetric heat generation	W m^{-3}
q_{pol}	polarization volumetric heat generation	W m^{-3}
q_{rea}	Reaction volumetric heat generation	W m^{-3}
Q	charge capacity (10^3C ≈ 0.27Ah)	Ah
R	gas constant (8.314 J mol^{-2} K^{-1})	J mol^{-2} K^{-1}
r	radius distance variable of electrode particles	m

r_0	radius of electrode particles	m
S	entropy	J K^{-1}
S_a	specific surface area	m^{-1}
t	time	s
t^+	Li^+ transference number	
T	temperature	K
T_{amb}	ambient temperature	K
U_{eq}	open circuit potential of the electrode	V
$U_{eq,ref}$	open circuit potential under the reference temperature	V
ν_l	thermodynamic factor of the electrolyte	

Greek letters

α	convective heat transfer coefficient	W m^{-2} K^{-1}
α_a	anodic transfer coefficient	
α_c	cathodic transfer coefficient	
ε	emissivity of the battery surface	
ε_s	active material volume fraction	
ε_l	electrolyte volume fraction	
λ	thermal conductivity	W m^{-1} K^{-1}
ρ	density	kg m^{-3}
σ	Stephen-Boltzmann constant (5.67×10^{-8} W m^{-2} K^{-4})	W m^{-2} K^{-4}
σ_s	electronic conductivity in solid phase material	S m^{-1}
σ_l	ionic conductivity of electrolyte	S m^{-1}
ϕ_s	solid phase potential	V
ϕ_l	electrolyte phase potential	V
γ	Bruggeman tortuosity exponent	
δ_i	thickness of battery component	m
η	local surface over potential	V
Δ	change	
∇	divergence	

Subscripts and superscripts

0	initial or equilibrated value
p	positive electrode
n	negative electrode
s	solid phase
l	liquid/electrolyte phase
amb	ambient
eff	effective value
max	maximum
ref	reference value
surf	surface of active material particles

References

[1] S. Panchal, I. Dincer, M. Agelin-Chaab, R. Fraser, M. Fowler, Experimental temperature distributions in a prismatic lithium-ion battery at varying conditions, Int. Commun. Heat Mass Transf. 71 (2016) 35–43. doi:10.1016/j.icheatmasstransfer.2015.12.004.

[2] Y. Tang, L. Wu, W. Wei, D. Wen, Q. Guo, W. Liang, L. Xiao, Study of the thermal properties during the cyclic process of lithium ion power batteries using the electrochemical-thermal coupling model, Appl. Therm. Eng. 137 (2018) 11–22. doi:10.1016/j.applthermaleng.2018.03.067.

[3] G. Guo, B. Long, B. Cheng, S. Zhou, P. Xu, B. Cao, Three-dimensional thermal finite element modeling of lithium-ion battery in thermal abuse application, J. Power Sources. 195 (2010) 2393–2398. doi:10.1016/j.jpowsour.2009.10.090.

[4] A. Kvasha, C. Gutiérrez, U. Osa, I. de Meatza, J.A. Blazquez, H. Macicior, I. Urdampilleta, A comparative study of thermal runaway of commercial lithium ion cells, Energy. 159 (2018) 547–557. doi:10.1016/j.energy.2018.06.173.

[5] P. Peng, F. Jiang, Thermal safety of lithium-ion batteries with various cathode materials: A numerical study, Int. J. Heat Mass Transf. 103 (2016) 1008–1016. doi:10.1016/j.ijheatmasstransfer.2016.07.088.

[6] X. Feng, M. Ouyang, X. Liu, L. Lu, Y. Xia, X. He, Thermal runaway mechanism of lithium ion battery for electric vehicles: A review, Energy Storage Mater. 10 (2018) 246–267. doi:10.1016/j.ensm.2017.05.013.

[7] S. Zheng, L. Wang, X. Feng, X. He, Probing the heat sources during thermal runaway process by thermal analysis of different battery chemistries, J. Power Sources. 378 (2018) 527–536. doi:10.1016/j.jpowsour.2017.12.050.

[8] S. Abada, M. Petit, A. Lecocq, G. Marlair, V. Sauvant-Moynot, F. Huet, Combined experimental and modeling approaches of the thermal runaway of fresh and aged lithium-ion batteries, J. Power Sources. 399 (2018) 264–273. doi:10.1016/j.jpowsour.2018.07.094.

[9] C. Qi, Y. Zhu, F. Gao, K. Yang, Q. Jiao, Mathematical model for thermal behavior of lithium ion battery pack under overcharge, Int. J. Heat Mass Transf. 124 (2018) 552–563. doi:10.1016/j.ijheatmasstransfer.2018.03.100.

[10] M. Parhizi, M.B. Ahmed, A. Jain, Determination of the core temperature of a Li-ion cell during thermal

runaway, J. Power Sources. 370 (2017) 27–35. doi:10.1016/j.jpowsour.2017.09.086.

[11] Z. An, L. Jia, L. Wei, C. Dang, Q. Peng, Investigation on lithium-ion battery electrochemical and thermal characteristic based on electrochemical-thermal coupled model, Appl. Therm. Eng. 137 (2018) 792–807. doi:10.1016/j.applthermaleng.2018.04.014.

[12] M. Doyle, Modeling of Galvanostatic Charge and Discharge of the Lithium/Polymer/Insertion Cell, J. Electrochem. Soc. (1993). doi:10.1149/1.2221597.

[13] D. Bernardi, E. Pawlikowski, J. Newman, A General Energy Balance for Battery Systems, J. Electrochem. Soc. 132 (1985) 5. doi:10.1149/1.2113792.

[14] N. Baba, H. Yoshida, M. Nagaoka, C. Okuda, S. Kawauchi, Numerical simulation of thermal behavior of lithium-ion secondary batteries using the enhanced single particle model, J. Power Sources. 252 (2014) 214–228. doi:10.1016/j.jpowsour.2013.11.111.

[15] K. Somasundaram, E. Birgersson, A.S. Mujumdar, Thermal-electrochemical model for passive thermal management of a spiral-wound lithium-ion battery, J. Power Sources. 203 (2012) 84–96. doi:10.1016/j.jpowsour.2011.11.075.

[16] X. Zhang, Thermal analysis of a cylindrical lithium-ion battery, Electrochim. Acta. 56 (2011) 1246–1255. doi:10.1016/j.electacta.2010.10.054.

[17] M. Farag, H. Sweity, M. Fleckenstein, S. Habibi, Combined electrochemical, heat generation, and thermal model for large prismatic lithium-ion batteries in real-time applications, J. Power Sources. 360 (2017) 618–633. doi:10.1016/j.jpowsour.2017.06.031.

[18] Y. Ye, Y. Shi, N. Cai, J. Lee, X. He, Electro-thermal modeling and experimental validation for lithium ion battery, J. Power Sources. 199 (2012) 227–238. doi:10.1016/j.jpowsour.2011.10.027.

[19] S.C. Chen, C.C. Wan, Y.Y. Wang, Thermal analysis of lithium-ion batteries, J. Power Sources. 140 (2005) 111–124. doi:10.1016/j.jpowsour.2004.05.064.

[20] D.H. Jeon, S.M. Baek, Thermal modeling of cylindrical lithium ion battery during discharge cycle, Energy Convers. Manag. 52 (2011) 2973–2981. doi:10.1016/j.enconman.2011.04.013.

[21] Y. Inui, Y. Kobayashi, Y. Watanabe, Y. Watase, Y. Kitamura, Simulation of temperature distribution in cylindrical and prismatic lithium ion secondary batteries, Energy Convers. Manag. 48 (2007) 2103–2109. doi:10.1016/j.enconman.2006.12.012.

[22] D.H. Jeon, Numerical modeling of lithium ion battery for predicting thermal behavior in a cylindrical cell, Curr. Appl. Phys. 14 (2014) 196–205. doi:10.1016/j.cap.2013.11.006.

[23] S. Panchal, I. Dincer, M. Agelin-Chaab, R. Fraser, M. Fowler, Experimental and theoretical investigation of temperature distributions in a prismatic lithium-ion battery, Int. J. Therm. Sci. 99 (2016) 204–212. doi:10.1016/j.ijthermalsci.2015.08.016.

[24] N. Damay, C. Forgez, M.P. Bichat, G. Friedrich, Thermal modeling of large prismatic LiFePO4/graphite battery. Coupled thermal and heat generation models for characterization and simulation, J. Power Sources. 283 (2015) 37–45. doi:10.1016/j.jpowsour.2015.02.091.

[25] S. Du, Y. Lai, L. Ai, L. Ai, Y. Cheng, Y. Tang, M. Jia, An investigation of irreversible heat generation in lithium ion batteries based on a thermo-electrochemical coupling method, Appl. Therm. Eng. 121 (2017) 501–510. doi:10.1016/j.applthermaleng.2017.04.077.

[26] Z. Wang, J.U.N. Ma, L.E.I. Zhang, Finite Element Thermal Model and Simulation for a Cylindrical Li-Ion Battery, 5 (2017).

[27] S. Panchal, I. Dincer, M. Agelin-Chaab, R. Fraser, M. Fowler, Thermal modeling and validation of temperature distributions in a prismatic lithium-ion battery at different discharge rates and varying boundary conditions, Appl. Therm. Eng. 96 (2016) 190–199. doi:10.1016/j.applthermaleng.2015.11.019.

[28] Y. Ye, Y. Shi, A.A.O. Tay, Electro-thermal cycle life model for lithium iron phosphate battery, J. Power Sources. 217 (2012) 509–518. doi:10.1016/j.jpowsour.2012.06.055.

[29] J. Li, Y. Cheng, M. Jia, Y. Tang, Y. Lin, Z. Zhang, Y. Liu, An electrochemical-thermal model based on dynamic responses for lithium iron phosphate battery, J. Power Sources. 255 (2014) 130–143. doi:10.1016/j.jpowsour.2014.01.007.

[30] M. Xu, Z. Zhang, X. Wang, L. Jia, L. Yang, Two-dimensional electrochemical-thermal coupled modeling of cylindrical LiFePO4batteries, J. Power Sources. 256 (2014) 233–243. doi:10.1016/j.jpowsour.2014.01.070.

[31] L.H. Saw, Y. Ye, A.A.O. Tay, Electrochemical–thermal analysis of 18650 Lithium Iron Phosphate cell, Energy Convers. Manag. 75 (2013) 162–174. doi:10.1016/j.enconman.2013.05.040.

[32] M.S. Rad, D.L. Danilov, M. Baghalha, M. Kazemeini, P.H.L. Notten, Thermal Modeling of Cylindrical LiFePO4 Batteries, J. Mod. Phys. 04 (2013) 1–7. doi:10.4236/jmp.2013.47A2001.

[33] E. Prada, D. Di Domenico, Y. Creff, J. Bernard, V. Sauvant-Moynot, F. Huet, Simplified Electrochemical and Thermal Model of LiFePO4-Graphite Li-Ion Batteries for Fast Charge Applications, J. Electrochem. Soc. 159 (2012) A1508–A1519. doi:10.1149/2.064209jes.

[34] O. Capron, A. Samba, N. Omar, P. Van Den Bossche, J. Van Mierlo, Thermal behaviour investigation of a large and high power lithium iron phosphate cylindrical cell, Energies. 8 (2015) 10017–10042. doi:10.3390/en80910017.

[35] F. Bahiraei, M. Ghalkhani, A. Fartaj, G.A. Nazri, A pseudo 3D electrochemical-thermal modeling and analysis of a lithium-ion battery for electric vehicle thermal management applications, Appl. Therm. Eng. 125 (2017) 904–918. doi:10.1016/j.applthermaleng.2017.07.060.

[36] M. Xu, Z. Zhang, X. Wang, L. Jia, L. Yang, A pseudo three-dimensional electrochemical-thermal model of a prismatic LiFePO4battery during discharge process, Energy. 80 (2015) 303–317. doi:10.1016/j.energy.2014.11.073.

[37] A. Maheshwari, M.A. Dumitrescu, M. Destro, M. Santarelli, a Modelling Approach To Understand Charge Discharge Differences in Thermal Behaviour in Lithium Iron Phosphate – Graphite Battery, Electrochim. Acta. 243 (2017) 129–141. doi:10.1016/j.electacta.2017.05.049.

[38] Y. Lai, S. Du, L. Ai, L. Ai, Y. Cheng, Y. Tang, M. Jia, Insight into heat generation of lithium ion batteries based on the electrochemical-thermal model at high discharge rates, Int. J. Hydrogen Energy. 40 (2015) 13039–13049. doi:10.1016/j.ijhydene.2015.07.079.

[39] B. Wu, Y. Ren, N. Li, LiFePO 4 Cathode Material, Electr. Veh. – Benefits Barriers. (2011) 199–216. doi:10.5772/717.

[40] D. V. Safronov, I.Y. Pinus, I.A. Profatilova, V.A. Tarnopol'skii, A.M. Skundin, A.B. Yaroslavtsev, Kinetics of lithium deintercalation from LiFePO4, Inorg. Mater. 47 (2011) 303–307. doi:10.1134/S0020168511030198.

[41] V. Srinivasan, J. Newman, Discharge Model for the Lithium Iron-Phosphate Electrode, J. Electrochem. Soc. 151 (2004) A1517. doi:10.1149/1.1785012.

[42] J.L. Allen, T.R. Jow, J. Wolfenstine, Analysis of the FePO 4 to LiFePO 4 phase transition, J. Solid State Electrochem. 12 (2008) 1031–1033. doi:10.1007/s10008-007-0459-1.

[43] M. Mastali, M. Farkhondeh, S. Farhad, R.A. Fraser, M. Fowler, Electrochemical Modeling of Commercial LiFePO4 and Graphite Electrodes: Kinetic and Transport Properties and Their Temperature Dependence, J. Electrochem. Soc. 163 (2016) A2803–A2816. doi:10.1149/2.1151613jes.

[44] J.L. Dodd, Phase Composition and Dynamical Studies of Lithium Iron Phosphate, Discovery. 2007 (2007).

[45] V. Srinivasan, C.Y. Wang, Analysis of Electrochemical and Thermal Behavior of Li-Ion Cells, J. Electrochem. Soc. 150 (2003) A98. doi:10.1149/1.1526512.

[46] S.-C. Chen, Y.-Y. Wang, C.-C. Wan, Thermal Analysis of Spirally Wound Lithium Batteries, J. Electrochem. Soc. 153 (2006) A637. doi:10.1149/1.2168051.

[47] A123-SYSTEMS, 26650 Production Change Model ANR26650M1A to Model ANR26650M1B, 2011.

[48] Keysight Technologies, Making High-Accuracy Temperature Measurements with the 34970A and 34972A Data Acquisition SwitchUnits, 2017.

[49] V. V. Viswanathan, D. Choi, D. Wang, W. Xu, S. Towne, R.E. Williford, J.G. Zhang, J. Liu, Z. Yang, Effect of entropy change of lithium intercalation in cathodes and anodes on Li-ion battery thermal management, J. Power Sources. 195 (2010) 3720–3729. doi:10.1016/j.jpowsour.2009.11.103.